ACS APPLIED MATERIALS & INTERFACES

Letter

www.acsami.org

# ZnO Anchored on Vertically Aligned Graphene: Binder-Free Anode Materials for Lithium-Ion Batteries

N. Li, S. X. Jin, Q. Y. Liao, and C. X. Wang*

State Key Laboratory of Optoelectronic Materials and Technologies, School of Physics Science and Engineering, Sun Yat-sen (Zhongshan) University, Guangzhou 510275, People's Republic of China

Supporting Information

**ABSTRACT:** ZnO has been regarded as a promising anode material for the next-generation lithium-ion battery. Unfortunately, the structure broken caused by the volume change of ZnO and the capacity degression due to the irreversible electrochemical reaction of ZnO still remain two major challenges. Here, we design a novel kind of in situ growth binder-free ZnO-based anodes via ZnO anchored on vertically aligned graphene. The composite anode retains physical integrity post cycling. Especially, the good conductivity of graphene and the ultrasmall size of ZnO particles help to produce a completely reversible electrochemical reaction of ZnO-based anode. The composite material exhibits a high capacity (810 mAh $g^{-1}$), long cycle life, good cycle stability, and fast charge/discharge rate.

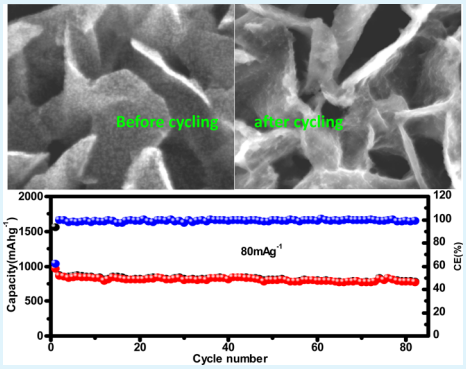


**KEYWORDS:** *ZnO, vertically aligned graphene, reversion reaction, lithium-ion battery*

With the development of science and technology, new kinds of energy conversion and storage devices such as solar cell, fuel cell, lithium-ion battery (LIB,) and supercapacitor are appreciated.[1−5] Among which, LIB with the applications from small-scale portable electronic devices to large-scale electric vehicles, is regarded as one of the most promising representatives of the main power source.[6−9] As a result, the materials with high theoretical capacities such as silicon (4200 mAh $g^{-1}$),[10,11] germanium (1620 mAh $g^{-1}$)[12,13]tin (990 mAh $g^{-1}$)[14,15] were studied extensively. Unfortunately, the complete nontoxicity, low cost, easy preparation, and chemical stability of ZnO has attracted little attention because of its unstable cycling property though it poses a fairish theoretical capacity 978 $mAhg^{-1}$.[16,17] The poor electrical conductivity and the large volume change (about 300%),[18−20] which will cause large intrinsic resistance, severe disintegration of electrode and electrical disconnection between active materials and current collector, are two important reasons for the capacity fading and unstable cycle capability of ZnO.

Lots of efforts centered on enhancing the electrical conductivity and stabilizing of anode structures have been attempted. Different designs can be classified into two main groups: (1) Proceeding from stabilizing of ZnO structures, active materials were prepared into nanostructures.[16,17,19−30] (2) Proceeding from enhancing the electrical conductivity, ZnO-based carbon or some metal composite materials were used as anodes.[18,24,25,29−35] Here, we design a structure that could solve both the poor electrical conductivity and the volume change induced electrode disintegration problems. As shown in Figure 1e, in situ grown ultrathin graphene sheets vertically aligned on copper foil current collector. ZnO nanoparticles (ZnO-NPs) uniformly anchored on both sides of the vertically aligned graphene sheets (ZnO-VAGN). Within this design, some special features are analyzed as follows. First, ZnO was prepared into nanosized structures to avoid pulverization by reducing the absolute volume change. Second, the direct growth of the VAGN phase offers some advantages: (i) each ultrathin VAGN is electrically connected to the Cu current collector with a distance of about 1−2 $\mu$m apart from each other, which preventing the VAGNs from restacking with one another, such that the entire ZnO-VAGN phase contributes to the capacity. (ii) ZnO nanoparticles uniformly anchored on integral graphene sheets, thereby both sides of a single sheet in the VAGN composites were fully used and the freestanding graphene-ZnO sheets could supply direct 2D-in-plane pathways allowing for efficient charge transport to shorten the Li-ion transport pathway. In addition, the 3−6 nm nanoparticles (the statistic results was given in the Supporting Information, Figure S1a, and Histogram S1) uniformly anchored on both sides of VAGNs, and the distance between them could supply enough expansion space for ZnO nanoparticles during cycle process. Namely, the ZnO nanoparticles will still remain on the surface of VAGNs even after it pulverized into smaller ones during the cycling process. In fact, these speculations were confirmed in the TEM test of the anodes after cycling. (iii) The good conductivity of graphene

Received: October 13, 2014
Accepted: November 14, 2014
Published: November 14, 2014

  

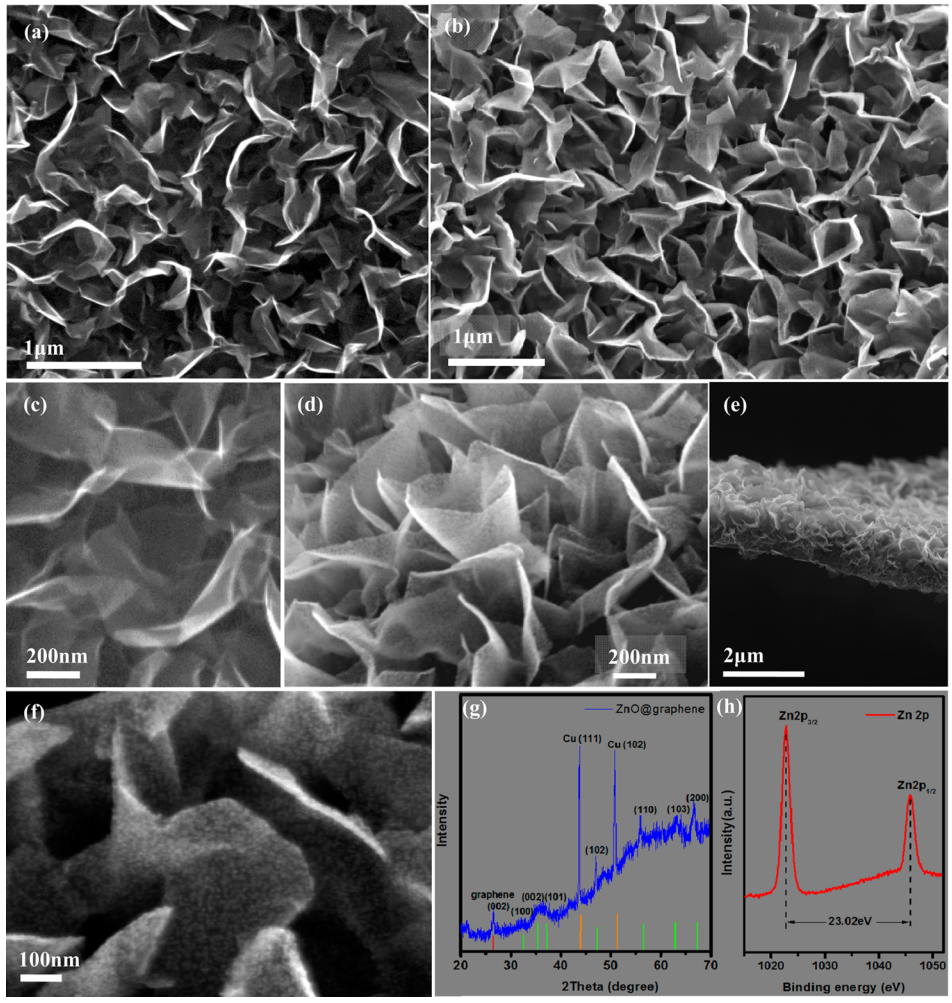


**Figure 1.** Morphology characterizations (SEM images) of (a) pure VAGNs and (b) ZnO-VAGNs. High-resolution SEM micrographs of (c) pure VAGNs and (d, f) ZnO-VAGNs. (e) Sectional view of ZnO-VAGNs grown on Cu current collector. (g) X-ray diffraction (XRD) pattern of the ZnO-VAGNs. (h) XPS spectrum of Zn 2p3/2 in ZnO-VAGNs.

and the ultrasmall size of ZnO particles help to produce a completely reversible electrochemical convertion reaction of ZnO-based anode. The simple special structure of ZnO composite contributes a lot to its enhanced electromechanical performance. The electrodes exhibit (1) a high reversible capacity value of 810 mAh $g^{-1}$ at 80 mA $g^{-1}$, (2) cycle lives of more than 105 times with a capacity loss of about 6.0%, and (3) a retained capacity of 201 mAh $g^{-1}$ with a discharge time of 40s.

The synthesis of the freestanding graphene sheets was performed in a microwave plasma enhanced chemical vapor deposition system (MPECVD) equipped, and ZnO nanoparticles were added through hydro-thermal synthesis method. SEM micrograph in Figure 1a indicates that the VAGNs were arbitrarily interlaced, with each two sheets in the range of hundreds of nanometers, which is sufficiently wide to prevent them restacking with one another. The growth process was described in our previous reports. As illustrated in Figure 1b, there are no significant differences between the low-resolution SEM images of VAGNs and ZnO-VAGN composites because of the ultrasmall size of the ZnO-NPs and their monolayer dispersion. The high-resolution SEM micrographs clearly display the pure graphene sheets with smooth surface(Figure 1c) and ZnO-based graphene sheets anchored with a series of nanosized, regularly arranged and well-dispersed ZnO particles (Figure 1d, f). The sectional view of the ZnO-VAGNs in Figure 1e demonstrates that composite sheets grown vertically to and tightly adhered with the current collector. The anode ZnO-VAGNs grown on Cu was directly characterized by XRD. The XRD profile in Figure 1g demonstrates that all the diffraction peaks and their relative intensities coincide with the JCPDS card no. 36−1451. It should be noted here that the full width at half-maximum (fwhm) of the first three diffraction peaks were too wide to distinguish due to the size effect of the ultrasmall ZnO particles. The XPS spectrum of Zn 2P in Figure 1h further indicates the success in synthesis of ZnO nanoparticles. The crystal structure and phase analysis of the composites were corresponding to the observations in TEM micrographs.

TEM micrographs illustrate the structure details of a single pure graphene and an integrate ZnO-VAGN sheet. As shown in Figure 2a and Figure S2a, b in the Supporting Information, some defects can be identified which are considered to be beneficial for the nucleation and growth of ZnO nanoparticles. The mass proportion of ZnO to the composite can be greatly improved, which will contribute significantly to the improved capacity. These defects that usually arise from vacancies, distortions, corrugation, and edges could also be confirmed by the Raman spectrum in Figure S2 in the Supporting Information. The growth model of the defects was explained

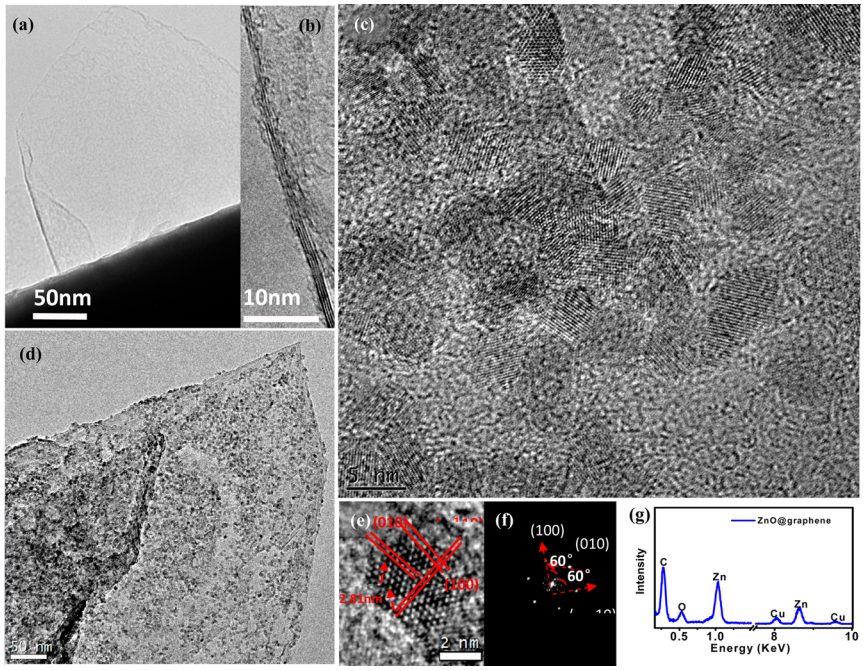


**Figure 2.** Structure characterizations (TEM images) of ZnO-VAGNs composite: (a) low- and (b) high-resolution TEM images of an integrity graphene nanosheet. (c) High- and (d) low-resolution TEM micrographs of a single graphene nanosheet anchored with ZnO nanoparticles. (e) High-resolution TEM micrograph of a single ZnO nanoparticle, and (f) the corresponding FFT transformation. (g) Energy-dispersive X-ray spectroscopy (EDS) analysis of ZnO-VAGNs.

in Figure S3 in the Supporting Information. Approximately three to five dark lines with an intermediate distance of 0.364 nm can be observed in Figure 2b, identified as two to four layers of graphene sheets.

Post the ZnO growing process, a monolayer of ZnO nanoparticles dispersed on a single entire graphene sheet as illustrated in the low-magnification of ZnO-VAGNs in Figure 2d. The statistics of the size dispersion of the ZnO-NPs in Table S1 and Histogram S1 in the Supporting Information demonstrated that the diameters of ZnO-NPs are mainly sized 3.5−4.5 nm. The high-resolution TEM image in Figure 2c indicated that the ZnO nanoparticles uniformly anchored on graphene, no agglomeration existed, whereas the lattice spacing of 0.28 nm appeared in three directions with included angles of 60°, corresponding to hexagonal crystal structure of ZnO (Figure 2e). In addition, the energy-dispersive X-ray spectroscopy (EDS) analysis shows that the ZnO-VAGNs is mainly composed of Zn, O, and C, which is in accord with the presence of both ZnO-VAGNs in the hybrid.

The electrical performance behaviors of the ZnO-VAGNs anodes were tested by cyclic voltammetry, with the resulting cyclic voltammograms ($C-V$) presented in Figure 3a, a voltage range from 0.01 to 3 V and a sweep rate of 0.1 mV/s were employed to gain a better understanding of the electrochemical reaction mechanism in the full voltage range. Ten cycles were recorded. The oxido-reduction peaks in the second and third charge and discharge cycles were found to be similar, whereas different peaks appeared in the first one. In the first cathodic cycle, a reduction peak appeared at 1.25 V was caused by the decomposition of electrolyte and the formation of solid electrolyte interphase (SEI) layers.[24,36,37] This peak disappeared in the following cycles, and was regarded as one reason for the irreversible capacity. The wide peak at 0.5−0.75 V was the first electrochemical process of the active material-ZnO. This process includes three electrochemical reactions, ZnO was reduced into Zn and meanwhile the SEI layer formed (0.75 V), Zn alloyed with Li and formed into $Zn_xLi_y$ (0.5 V). Another reversible peak as low as 0.1 V corresponds to the reaction that the intercalation of lithium into the graphene layers. Three peaks appeared in the first anodic cycle, the first peak at 0.1 V was ascribed to the delithiation of graphene layer, and the second wide peak located at 1.25−1.75 V was caused by the possible multistep dealloying process $Zn_xLi_y$. The important third peak at 2.25 V corresponds to the reversible convention reaction between Zn and ZnO, which remains in the following cycles, indicating a high capacity and stable cycle property. During the following cycles, the shapes of the curves remain almost the same, verifying the good capacity retention.

Charge and discharge curves for a few typical cycles acquired at 80 mA $g^{-1}$ and 0−2.5 V are presented in Figure 3b to describe the discharge voltage plateau position and capacity. Obviously, the plateaus on the voltage profiles coincide with the peaks in C−V curve. An obvious slop located between 0.3 and 1.0 V appears in the first discharge cycle. This slop contains an irreversible capacity caused by the formation of SEI film and the electrochemical conversion reaction processes of ZnO correspond to the peaks 1.25 V, 0.5−0.75 V in the $C-V$ curve. A short plateau at 0.1 V is related to the reversible reduction peak of the lithiation of graphene (0.1 V) in the $C-V$ curve. The plateaus of delithiation of $C_xLi_y$ and $Zn_xLi_y$ occurred at 0.05−0.2 V and 1.0−1.4 V, respectively. The short but important plateau at 2.25 V was ascribed to the reversible oxidation reaction of Zin related to the oxidation peak in the C−V curve. After the first cycle, the discharge capacity caused by the deformation of electrolyte disappeared, so the discharge plateau was a little shorter. The positions of other plateaus in the charge and discharge curves maintained unchanged, indicating good capacity retention. The ZnO-VAGNs delivers a first discharge capacity of 1560 mAh $g^{-1}$ and a first charge capacity of 955 mAh $g^{-1}$, the Coulombic efficiency is a little lower 61.2%

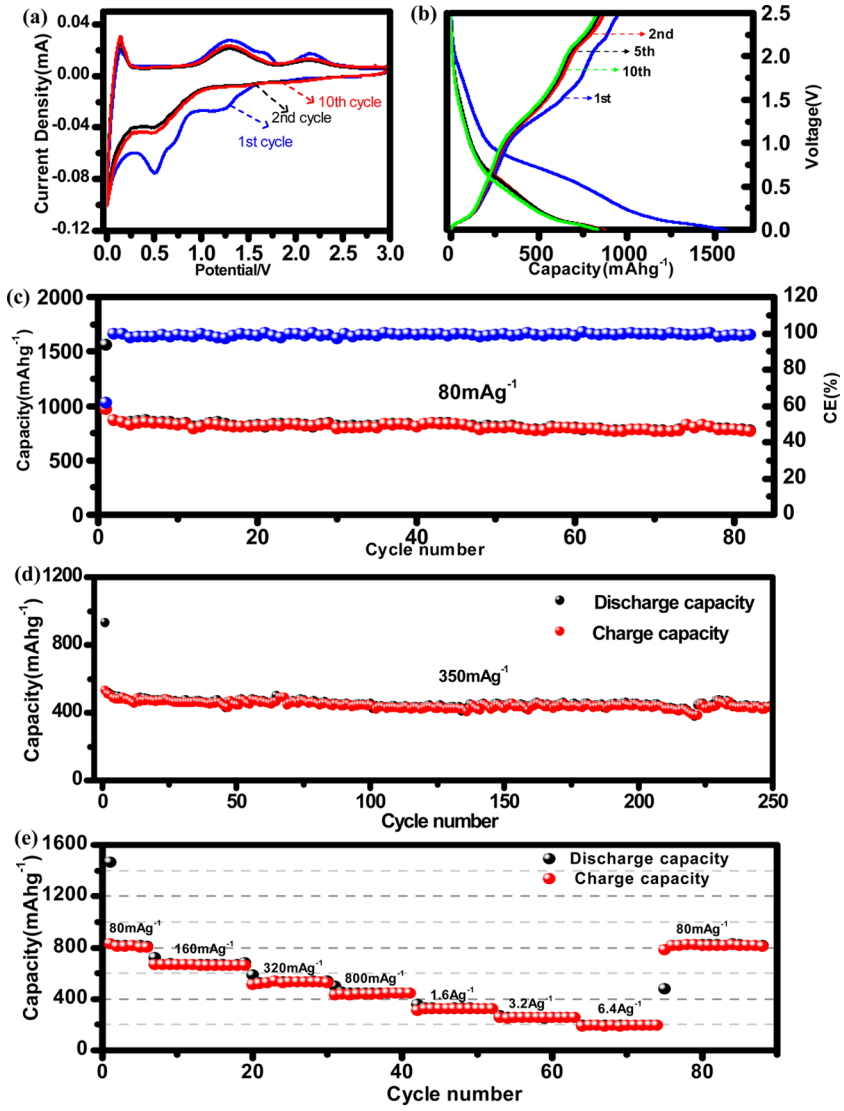


**Figure 3.** Electrochemical properties of ZnO-VAGNs in a voltage range of 0−2.5 V: (a) cyclic voltammetry (*C*−*V*) curves of the ZnO-VAGNs (vs $Li/Li^+$ at a scanning rate of 0.1 mV/s), (b) charge and discharge cycle curves of ZnO-VAGNs as anode in lithium cells at a current density of 80 $mAg^{-1}$, (c) capacity and Coulombic efficiency versus cycle number for ZnO-VAGNs at a current density of 80 $mAg^{-1}$, (d) capacity of ZnO-VAGNs anode versus cycle number cycled at 80 $mAg^{-1}$. (e) Capacity over cycling at different current densities.

because of the large surface area. The CE increases to 99.5% though the charge and discharge capacities decrease to 865 mAh $g^{-1}$ (16.87 mAh $m^{-2}$) and 869 mAh $g^{-1}$ in the second cycle. The capacity was a little higher than its estimated theoretical capacity of 791.5 mAh $g^{-1}$ (The theoretical capacity is calculated by assuming a mixture of ZnO and graphene: $C_{theoretical} = C_{ZnO\cdot\%mass\ of\ ZnO} + C_{Graphite\cdot\%mass\ of\ Graphite}$ = 978·0.68 + 372·0.32 = 768.8 mAh $g^{-1}$).[38] The weighing methods are given in the Supporting Information, Figure S5. Three factors mainly contribute to the capacity, the conversion reactions of ZnO with lithium, graphene with lithium; and the interfacial lithium storage. The charge and discharge curves of the fifth and tenth cycles almost coincide with each other, indicating good cycle stability.

The ZnO-VAGNs anode exhibit outstanding cycling stability at different current densities in a voltage of 0.001−2.5 V. As illustrated in Figure 3c, more than 100 cycles were accomplished at a current density of 80 mAh $g^{-1}$. The reversible capacity of the 10th, 50th, 100th cycles could still remain 834, 810, and 809 $mAhg^{-1}$, displaying good capacity retention. Despite the obvious decrease in the first three cycles, the capacity gradually becomes stable after 20 cycles at about 800 mAh $g^{-1}$. The Coulombic efficiency is always between 97.6 and 100% except for the first cycle 61.2%. The composite was further tested at a larger current density 350 mAh $g^{-1}$ to verify its good cycling stability. During the accomplished 250 cycles, the capacity decreases from 513 mAh $g^{-1}$ (2nd cycle) to 467 mAh $g^{-1}$ (20th cycle), 451 mAh $g^{-1}$ (50th cycle), and becoming stable after that except for some minor fluctuations. For comparison, pure VAGN was also cycled (see Figure S4b in the Supporting Information), the cycle stability was good but the capacity was poor, indicating that the VAGN was an appropriate choice as the supporter of ZnO-NPs.

The rate capability of the ZnO-VAGNs anode was evaluated by expending the cycling test beyond conventional current rate. As shown in Figure 3d, the ZnO-VAGNs anode was cycled at various current rates from 80 mA $g^{-1}$ to extremely high $6.4Ag^{-1}$ in the potential range of 0.001−2.5 V. At 80 mA $g^{-1}$, the discharge capacity (810 mAh $g^{-1}$) was a little lower than the theoretical capacity of pure ZnO 978 mAh $g^{-1}$ and was


dx.doi.org/10.1021/am507046k | ACS Appl. Mater. Interfaces 2014, 6, 20590−20596

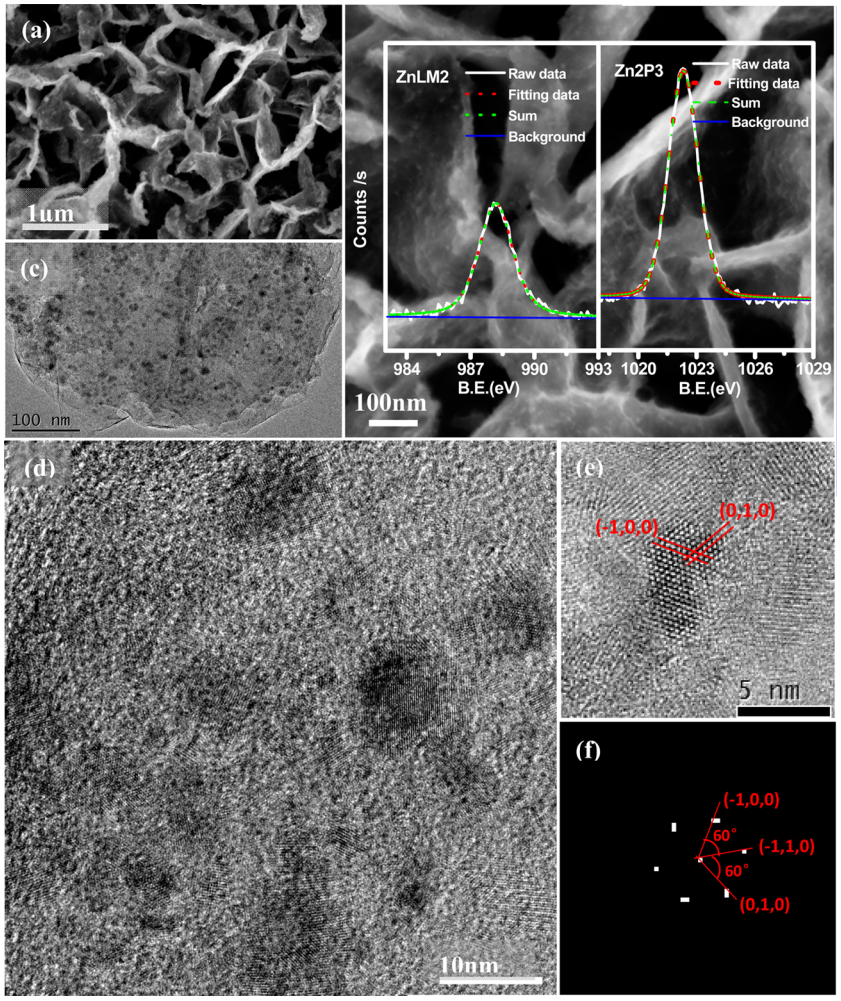


**Figure 4.** Morphology and structure analysis of ZnO-VAGNs post cycling for 100 cycles at fully charged state 2.5 V. (a, b) Low- and high-resolution SEM micrographs of ZnO-VAGNs post cycling. The inset in (b) XPS spectrum of Zn 2p3/2 and ZnLM2 in ZnO-VAGNs post cycling. (c, d) Low- and high-resolution TEM micrographs of an integrate ZnO-VAGNs sheet post cycling. (e, f) High-resolution TEM micrograph of a single nanoparticle, and the corresponding FFT transformation.

comparable to estimated theoretical capacity of the composite 791.5 mAh $g^{-1}$ as mentioned above. The ZnO-VAGNs anode maintains a significant discharge capacity (201 mAh $g^{-1}$) even at 6.4 A $g^{-1}$, and an entire charge or discharge process requires only 40 s, which is comparable to the time required for supercapacitors, suggesting a promising electrode material for both LIB and supercapacitor applications. The capacity recovered when it reduced back to the corresponding initial current density value, indicating good capacity retention.

The enhanced electrochemical performance, i.e., high rate capacity, long cycle life, and enhanced capacity retention (cycle stability), were in good agreement with our expectations for the performance of the ZnO-VAGNs structure. Two important factors may relate to the good performance: (1) the size effect of the active material (ZnO-NPs) enhanced the capacity retention rate. Compared with larger size particles, the ultrasmall ZnO particles could supply short transport pathways for $Li^+$ to fully react with ZnO nanoparticles, namely, the reversible reaction was promoted and all the active materials could take effect. (2)The reversible interfacial lithium storage process was another factor that improved the capacity retention rate. As the analysis in the Supporting Information (Figure S4a), the capacity contribution from the VAGNs and the interfacial lithium storage almost remained the same due to the stable and unbroken physical structure.

To further understand the excellent battery characteristics, the morphological and structural changes of ZnO-VAGNs anode were studied post cycling for 100 cycles at fully charged state. The SEM mircographs in Figure 4a, b illustrated that the surface of ZnO-VAGNs was much rougher after charging with $Li^+$ due to the contamination of solid electrolyte interface (SEI) layer, and the average thickness of composite sheets increased to several nanometers. In addition, the produced SEI film may serve as a protective membrane to buffer the volume change during lithiation and delithiation process.[39,40] Despite the surface and thickness changes, the ZnO-VAGNs remained intact without breaking into small pieces. Instead of restack, the ZnO-VAGNs still vertically aligned on the current collector and appeared to remain in contact well with it. The low resolution TEM images in Figure 4c further verified that the graphene sheet remains integrate and the nanoparticles still uniformly distributed post cycling. Remarkably, the active particles returned back to the initial ZnO-NPs as shown in the HRTEM image (Figure 4d–f) and its selected area electron diffraction (see Figure S6 in the Supporting Information), which revealing a hexagonal structure of ZnO-NPs. The


dx.doi.org/10.1021/am507046k | ACS Appl. Mater. Interfaces 2014, 6, 20590–20596

reversible reaction process could be described as follows: (1) $ZnO + 2Li \rightarrow Zn + Li_2O$, (2) $Zn + Li \rightarrow LiZn$, (3) $LiZn \leftrightarrow Zn + Li$, (4) $Zn + Li_2O \leftrightarrow ZnO + 2Li$. This analysis was consistent with the XPS result of the composite post cycling. As illustrated in the inset spectrum of Figure 4b, the XPS spectrum of Zn 2P sufficiently attests the success in oxidation conversion of the active material into a high valence zinc oxide (ZnO) state. The fully returned oxidation state may be ascribed to the small size effect of ZnO nanoparticle, which was an indispensible reason for the enhanced capacity and high capacity retention.

In a word, a vertically aligned ZnO-Graphene composite structure was fabricated via a facile two-step method. VAGNs directly grown on Cu current collectors act as supporters for ZnO nanoparticles and largely enhance their conductivity. ZnO nanoparticles with a size of 3−6 nm uniformly anchored on both sides of graphene. ZnO-VAGNs composites were used as anode in LIB without adhesives and other complex brushing process of the active material. The composite material exhibits a high capacity, long cycle life, good cycle stability, and fast charge/discharge rate. The vertically aligned structure of the composites, which could provide large efficient areas, good conductivity, short transportation length for both lithium ions and electrons, and ZnO particles small enough to accomplish the fully reversible electrochemical reaction, contributes to its notable performance.

## ■ ASSOCIATED CONTENT

### Supporting Information

Detailed experimental process and additional references. This material is available free of charge via the Internet at http://pubs.acs.org.

## ■ AUTHOR INFORMATION

### Corresponding Author

*E-mail: wchengx@mail.sysu.edu.cn.

### Notes

The authors declare no competing financial interest.

## ■ ACKNOWLEDGMENTS

This work was financially supported by the National Nature Science Foundation of China (51125008, 11274392, U1401241).

## ■ REFERENCES

(1) Armand, M.; Tarascon, J. M. Building better batteries. *Nature* **2008**, *451*, 652−657.

(2) Kang, K. S.; Meng, Y. S.; Breger, J.; Grey, C. P.; Ceder, G. Electrodes with High Power and High Capacity for Rechargeable Lithium Batteries. *Science* **2006**, *311*, 977−980.

(3) Thomas, J. Lithium Batteries—A Spectacularly Reactive Cathode. *Nat. Mater.* **2003**, *2*, 705−706.

(4) Chen, C. J.; Hu, X. L.; Jiang, Y.; Yang, Z.; Hu, P.; Huang, Y. H. TiO2-B Nanosheets/Anatase Nanocrystals Co-Anchored on Nanoporous Graphene: In Situ Reduction-Hydrolysis Synthesis and Their Superior Rate Performance as an Anode Material. *Chem.—Eur. J.* **2014**, *20*, 1383−1388.

(5) Zou, F.; Hu, X. L.; Qie, L.; Jiang, Y.; Xiong, X. Q.; Qiao, Y.; Huang, Y. H. Facile Synthesis of Sandwiched $Zn_2GeO_4$-Graphene Oxide Nanocomposite as a Stable and High-Capacity Anode for Lithium-Ion Batteries. *Nanoscale* **2014**, *6*, 924−930.

(6) Goodenough, J. B. Evolution of Strategies for Modern Rechargeable Batteries. *Acc. Chem. Res.* **2012**, *46*, 1053−1061.

(7) Burke, A. Ultracapacitors: Why, How, and Where is the technology. *J. Power Sources* **2000**, *91*, 37−50.

(8) Tarascon, J. M.; Armand, M. Issues and Challenges Facing Rechargeable Lithium Batteries. *Nature* **2001**, *414*, 359−367.

(9) Dresselhaus, M. S.; Thomas, I. L. Alternative Energy Technologies. *Nature* **2001**, *414*, 332−337.

(10) Wu, H.; Chan, G.; Choi, J. W.; Ryu, I.; Yao, Y.; McDowell, M. T.; Lee, S. W.; Jackson, A.; Yang, Y.; Hu, L. B.; Cui, Y. Stable Cycling of Double-Walled Silicon Nanotube Battery Anodes Through Solid-Electrolyte Interphase Control. *Nat. Nanotechnol.* **2012**, *7*, 309−314.

(11) Chan, C. K.; Peng, H. L.; Liu, G.; McIlwrath, K.; Zhang, X. F.; Huggins, R. A.; Cui, Y. High-Performance Lithium Battery Anodes Using Silicon Nanowires. *Nat. Nanotechnol.* **2008**, *3*, 31−35.

(12) Yoon, S.; Park, C. M.; Sohn, H. J. Electrochemical Characterizations of Germanium and Carbon-Coated Germanium Composite Anode for Lithium-Ion Batteries. *Electrochem. Solid St.* **2008**, *11*, A42−A45.

(13) Park, M. H.; Cho, Y.; Kim, K.; Kim, J.; Liu, M. L.; Cho, J. Germanium Nanotubes Prepared by Using the Kirkendall Effect as Anodes for High-Rate Lithium Batteries. *Angew. Chem., Int. Ed.* **2011**, *50*, 9647−9650.

(14) Winter, M.; Besenhard, J. O. Electrochemical Lithiation of Tin and Tin-Based Intermetallics and Composites. *Electrochim. Acta* **1999**, *45*, 31−50.

(15) Ji, L. W.; Tan, Z. K.; Kuykendall, T.; An, E. J.; Fu, Y. B.; Battaglia, V.; Zhang, Y. G. Multilayer Nanoassembly of Sn-Nanopillar Arrays Sandwiched Between Graphene Layers for High-Capacity Lithium Storage. *Energy Environ. Sci.* **2011**, *4*, 3611−3616.

(16) Huang, X. H.; Xia, X. H.; Yuan, Y. F.; Zhou, F. Porous ZnO Nanosheets Grown on Copper Substrates as Anodes for Llithium Iion Batteries. *Electrochim. Acta* **2011**, *56*, 4960−4965.

(17) Pan, Q. M.; Qin, L. M.; Liu, J.; Wang, H. B. Flower-like ZnO-NiO-C Films with High Reversible Capacity and Rate Capability for Lithium-ion Batteries. *Electrochim. Acta* **2010**, *55*, 5780−5785.

(18) Zheng, Z. F.; Gao, X. P.; Pan, G. L.; Bao, J. L.; Qu, J. Q.; Wu, F.; Song, D. Y. Synthesis and Electrochemical Lithium Insertion of The Rod-like ZnO. *Chin. J. Inorg. Chem.* **2004**, *20*, 488−492.

(19) Liu, X. H.; Wang, J. Q.; Zhang, J. Y.; Yang, S. G. Sol−Gel-Template Synthesis of ZnO Nanotubes and Its Coaxial Nanocomposites of $LiMn_2O_4$/ZnO. *Mater. Sci. Eng., A* **2006**, *430*, 248−253.

(20) Liu, J. P.; Li, Y. Y.; Huang, X. T., ZnO Nanoneedle Arrays Directly Grown on Bulk Nickel Substrate for Li Ion Battery Electrodes with Improved Performance. In *2008 2nd IEEE International Nanoelectronics Conference*; IEEE: Piscataway, NJ, 2008; Vol. *1−3*, pp 53−57.

(21) Liu, J. P.; Li, Y. Y.; Ding, R. M.; Jiang, J.; Hu, Y. Y.; Ji, X. X.; Chi, Q. B.; Zhu, Z. H.; Huang, X. T. Carbon/ZnO Nanorod Array Electrode with Significantly Improved Lithium Storage Capability. *J. Phys. Chem. C* **2009**, *113*, 5336−5339.

(22) Huang, X. H.; Wu, J. B.; Lin, Y.; Guo, R. Q. ZnO Microrod Arrays Grown on Copper Substrates as Anode Materials for Lithium Ion Batteries. *Int. J. Electrochem. Sc.* **2012**, *7*, 6611−6621.

(23) Kushima, A.; Liu, X. H.; Zhu, G.; Wang, Z. L.; Huang, J. Y.; Li, J. Leapfrog Cracking and Nanoamorphization of ZnO Nanowires during In Situ Electrochemical Lithiation. *Nano Lett.* **2011**, *11*, 4535−4541.

(24) Ahmad, M.; Shi, Y. Y.; Nisar, A.; Sun, H. Y.; Shen, W. C.; Wei, M.; Zhu, J. Synthesis of Hierarchical Flower-Like ZnO Nanostructures and Their Functionalization by Au nanoparticles for Improved Photocatalytic and High Performance Li-Ion Battery Anodes. *J. Mater. Chem.* **2011**, *21*, 7723−7729.

(25) Park, J. S.; Lee, J. M.; Hwang, S. K.; Lee, S. H.; Lee, H. J.; Lee, B. R.; Park, H. I.; Kim, J. S.; Yoo, S.; Song, M. H.; Kim, S. O. A ZnO/N-Doped Carbon Nanotube Nanocomposite Charge Transport Layer for High Performance Optoelectronics. *J. Mater. Chem.* **2012**, *22*, 12695−12700.

(26) Lee, C. W.; Seo, S. D.; Kim, D. W.; Park, S.; Jin, K.; Kim, D. W.; Hong, K. S. Heteroepitaxial Growth of ZnO Nanosheet Bands on $ZnCo_2O_4$ Submicron Rods Toward High-Performance Li Ion Battery Electrodes. *Nano Res.* **2013**, *6*, 348−355.

(27) Wang, C. W.; Ma, X. L.; Cheng, J. G.; Cao, X. Y.; Sun, J. T.; Zhou, Y. H. Synthesis of $LiNi_{0.9}Co_{0.1}O_2$ Cathode Material for Lithium Secondary Battery by a Novel Route. *Mater. Lett.* **2007**, *61*, 556−560.
(28) Yang, G. Z.; Song, H. W.; Cui, H.; Liu, Y. C.; Wang, C. X. Ultrafast Li-ion Battery Anode with Superlong Life and Excellent Cycling Stability from Strongly Coupled ZnO Nanoparticle/Conductive Nanocarbon Skeleton Hybrid Materials. *Nano Energy* **2013**, *2*, 579−585.
(29) Su, Q. M.; Dong, Z. M.; Zhang, J.; Du, G. H.; Xu, B. S., Visualizing the Electrochemical Reaction of ZnO Nanoparticles with Lithium by in Situ TEM: Two Reaction Modes are Revealed. *Nanotechnology* **2013**, *24* (25).
(30) Liu, X. H.; Liu, Y.; Kushima, A.; Zhang, S. L.; Zhu, T.; Li, J.; Huang, J. Y. In Situ TEM Experiments of Electrochemical Lithiation and Delithiation of Individual Nanostructures. *Adv. Energy. Mater.* **2012**, *2*, 722−741.
(31) Fu, L. J.; Liu, H.; Li, C.; Wu, Y. P.; Rahm, E.; Holze, R.; Wu, H. Q. Surface Modifications of Electrode Materials for Lithium Ion Batteries. *Solid State Sci.* **2006**, *8*, 113−128.
(32) Shen, X. Y.; Mu, D. B.; Chen, S.; Wu, B. R.; Wu, F. Enhanced Electrochemical Performance of ZnO-Loaded/Porous Carbon Composite as Anode Materials for Lithium Ion Batteries. *ACS Appl. Mater. Inter.* **2013**, *5*, 3118−3125.
(33) Motohashi, T.; Raveau, B.; Caignaert, V.; Pralong, V.; Hervieu, A.; Pelloquin, D.; Maignan, A. Spin Glass to Weak Ferromagnetic Transformation in A New Layered Cobaltite: Consequence of Topotactic Reactions With Water at Room Temperature. *Chem. Mater.* **2005**, *17*, 6256−6262.
(34) Xia, H.; Zhu, D. D.; Fu, Y. S.; Wang, X. CoFe2O4-Graphene Nanocomposite as A High-Capacity Anode Material for Lithium-Ion Batteries. *Electrochim. Acta* **2012**, *83*, 166−174.
(35) Fu, Y. S.; Wan, Y. H.; Xia, H.; Wang, X. Nickel Ferrite-Graphene Heteroarchitectures: Toward High-Performance Anode Materials For Lithium-Ion Batteries. *J. Power Sources* **2012**, *213*, 338−342.
(36) Zhou, G. M.; Wang, D. W.; Li, F.; Zhang, L. L.; Li, N.; Wu, Z. S.; Wen, L.; Lu, G. Q.; Cheng, H. M. Graphene-Wrapped $Fe_3O_4$ Anode Material with Improved Reversible Capacity and Cyclic Stability for Lithium Ion Batteries. *Chem. Mater.* **2010**, *22*, 5306−5313.
(37) Lou, X. W.; Chen, J. S.; Chen, P.; Archer, L. A. One-Pot Synthesis of Carbon-Coated $SnO_2$ Nanocolloids with Improved Reversible Lithium Storage Properties. *Chem. Mater.* **2009**, *21*, 2868−2874.
(38) Paek, S. M.; Yoo, E.; Honma, I. Enhanced Cyclic Performance and Lithium Storage Capacity of $SnO_2$/Graphene Nanoporous Electrodes with Three-Dimensionally Delaminated Flexible Structure. *Nano Lett.* **2009**, *9*, 72−75.
(39) Kim, E.; Son, D.; Kim, T. G.; Cho, J.; Park, B.; Ryu, K. S.; Chang, S. H. A Mesoporous/Crystalline Composite Material Containing Tin Phosphate for Use as the Anode in Lithium-Ion Batteries. *Angew. Chem., Int. Ed.* **2004**, *43*, 5987−5990.
(40) Feng, Z.; Hu, X. L.; Li, Z.; Qie, L.; Hu, C. C.; Zeng, R.; Jiang, Y.; Huang, Y. H. MOF-Derived Porous ZnO/$ZnFe_2O_4$/C Octahedra with Hollow Interiors for High-Rate Lithium-Ion Batteries. *Adv. Mater.* **2014**, *26*, 6622−6628.